International Journal of Nanomedicine

Dovepress
Taylor & Francis Group

Open Access Full Text Article

ORIGINAL RESEARCH

# Pearl Powder Fluorescent Carbon Dots Alleviate Neuroinflammation in Cerebral Ischemia/Reperfusion Through Suppression of Anxa2/NF-κB Signaling Pathway

Pongsigeraxi Borjigin[1], Caixia Deng[2], Rilaga Su[2], Juan Li[1], Ying Ying[3], Yingsong Chen[4], Tegexibaiyin Wang[5]

[1]College of Mongolian Medicine, Inner Mongolia Minzu University, Tongliao, Inner Mongolia Autonomous Region, People's Republic of China; [2]College of Mongolian Medicine, Inner Mongolia Medical University, Hohhot, Inner Mongolia Autonomous Region, People's Republic of China; [3]College of Chemical Materials, Inner Mongolia Minzu University, Tongliao, Inner Mongolia Autonomous Region, People's Republic of China; [4]National and Local Joint Mongolian Medicine R&D Engineering Center, Inner Mongolia Minzu University, Tongliao, Inner Mongolia Autonomous Region, People's Republic of China; [5]Affiliated Hospital, Inner Mongolia Minzu University, Tongliao, Inner Mongolia Autonomous Region, People's Republic of China

Correspondence: Yingsong Chen, National and Local Joint Mongolian Medicine R&D Engineering Center, Inner Mongolia Minzu University, Tongliao, Inner Mongolia Autonomous Region, 028000, People's Republic of China, Email Cys1979@126.com; Tegexibaiyin Wang, Affiliated Hospital, Inner Mongolia Minzu University, Tongliao, Inner Mongolia Autonomous Region, 028000, People's Republic of China, Email tegexibaiyin@yeah.net



**Purpose:** This study aimed to enzymatically synthesize pearl powder fluorescent carbon dots (PFCDs) and investigate their neuroprotective potential against cerebral ischemia/reperfusion injury (CIRI) by modulating the Anxa2/NF-κB signaling pathway.

**Methods:** PFCDs were synthesized through enzymatic digestion and characterized. Neuroprotective effects were assessed using an in vitro oxygen–glucose deprivation/reoxygenation (OGD/R) model in PC12 cells and a middle cerebral artery occlusion/reperfusion (MCAO/R) rat model. Cell viability, neurological function, cerebral infarct volume, and neuronal injury were evaluated. Expression of Anxa2/NF-κB signaling pathway proteins and inflammatory cytokines (TNF-α, IL-6, IL-1β) was analyzed by Western blot, immunofluorescence, and ELISA.

**Results:** The synthesized PFCDs exhibited an organic–inorganic hybrid structure, uniform particle size below 10 nm, and distinctive optical properties. In vitro, PFCDs enhanced cell viability under OGD/R conditions, inhibited phosphorylation of Anxa2 and NF-κB p65, and reduced secretion of pro-inflammatory cytokines (TNF-α, IL-6, IL-1β). In vivo, treatment with PFCDs in MCAO/R rats improved neurological function, reduced cerebral infarct volume, and alleviated neuronal injury. These protective effects were linked to downregulation of the Anxa2/NF-κB signaling pathway and reduced serum levels of inflammatory cytokines.

**Conclusion:** We successfully achieved the enzymatic synthesis of carbon dots from pearl powder, characterized by a unique organic–inorganic hybrid structure. PFCDs effectively alleviated CIRI-induced neuroinflammation by suppressing the Anxa2/NF-κB signaling pathway, highlighting their therapeutic potential as a nanomedicine derived from natural products.

**Keywords:** pearl powder fluorescent carbon dots, cerebral ischemia/reperfusion, oxygen–glucose deprivation/reoxygenation, middle cerebral artery occlusion/reperfusion, neuroinflammation, Anxa2/NF-κB signaling pathway

## Introduction

Ischemic stroke (IS), which accounts for approximately 87% of all strokes, remains a major contributor to mortality and long-term disability worldwide.[1] Reperfusion therapy has marked a milestone in acute cerebral infarction management; however, in certain patients, re-establishing cerebral blood flow through recombinant tissue-type plasminogen activator (rt-PA) thrombolysis or interventional thrombectomy leads to aggravated brain injury. This phenomenon, known as cerebral ischemia/reperfusion (CIRI) injury, involves multiple pathological processes, including oxidative stress, autophagy, inflammation, and glial cell activation.[2,3] However, less than 5% of patients benefit from tissue plasminogen activator (tPA) due to its narrow therapeutic window and high bleeding risk, and approximately 30% of survivors experience neurological deficits caused by ischemia-

https://doi.org/10.2147/IJN.S567974
Received: 19 September 2025
Accepted: 30 January 2026
Published: 11 March 2026

**Graphical Abstract**

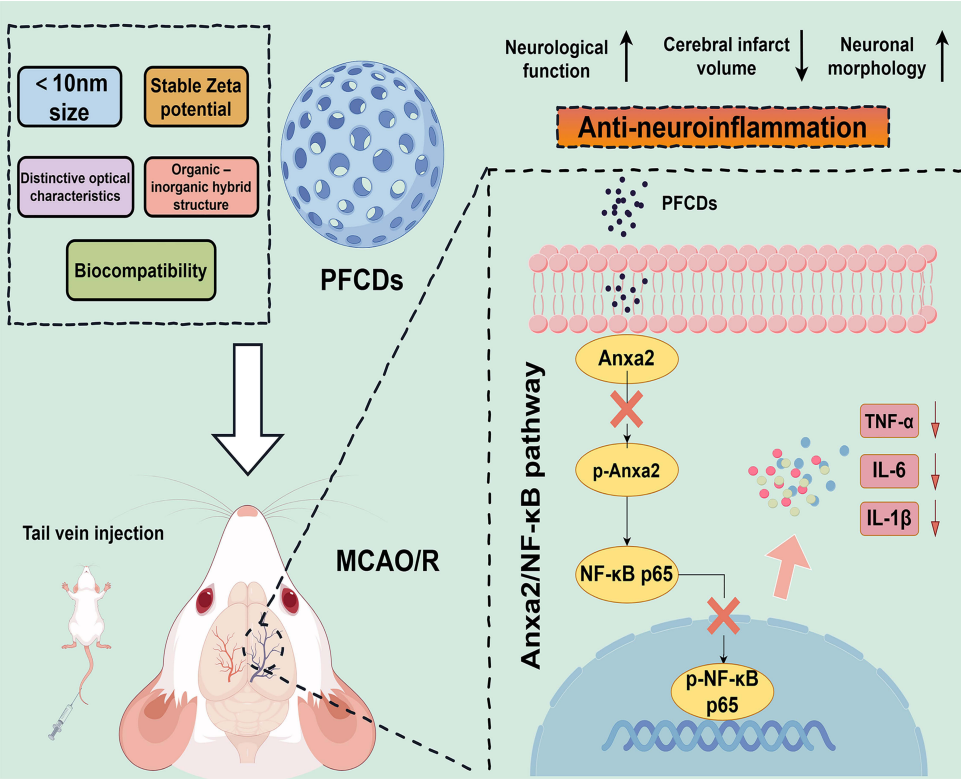


reperfusion injury.[4,5] Despite this, no effective drug currently exists to protect against CIRI injury, emphasizing the need to clarify its mechanisms and develop effective treatment strategies.[6] Nanomedicine, with its ability to cross the blood-brain barrier (BBB) and selectively target the ischemic penumbra surrounding the infarct core, has emerged as a promising approach for cerebrovascular diseases.[7,8] Carbon dots (CDs), a novel class of carbon nanomaterials following graphene, carbon nanotubes, and fullerenes, have attracted considerable attention for biotherapeutic applications. Their ultra-small size (<10 nm), stable surface charge, diverse functional chemical moieties, and favorable biocompatibility contribute to their biomedical potential[9,10] Previous studies indicate that CDs are non-toxic to tissues, organs, or genetic material.[11] Various natural sources, including straw, ginger, coffee, candle ash, eggs, and graphene, have been used for CD synthethis.[12,13] Notably, CDs have demonstrated antioxidant activity and inhibitory effects against hepatocellular, lung, breast, and cervical cancers.[11,14]

In this study, we developed and reported a novel method for the preparation of CDs derived from pearl powder. To the best of our knowledge, the enzymatic synthesis of carbon dots from pearl powder has not been previously described in the literature. Pearl powder originates from bivalve mollusks, where epithelial cells secrete calcium carbonate to encapsulate foreign substances. Its composition is dominated by inorganic calcium carbonate crystals (~95 wt%), with a small but essential proportion of organic matter (~5 wt%), including proteins and polysaccharides, which govern biomineralization and contribute to its biological activity.[15] Modern studies have demonstrated that pearl powder enhances immunity, exhibits anti-inflammatory and anti-aging effects, promotes central inhibition, improves skin appearance, and serves as a calcium supplement.[16] Owing to its fine particle dimensions and extensive surface area, pearl powder shows high bioavailability, facilitating the release and absorption of active ingredients.[17] Evidence further indicates that particle size influences therapeutic efficacy, leading to the development of nano-pearl powder, which releases more active proteins with enhanced activity.[18] In this study, we employed enzymatic digestion to synthesize pearl powder fluorescent carbon dots (PFCDs), which exhibit excellent water solubility, fluorescence, and biocompatibility.[19]

Annexin A2 (Anxa2) is a multifunctional phospholipid-binding protein with $Ca^{2+}$ dependence, expressed in a wide range of cell types. It contributes to the development of atherosclerosis (AS) by regulating inflammatory pathways, endothelial homeostasis, and lipid metabolism.[20,21] Anxa2 deficiency is strongly associated with enhanced inflammatory responses. Notably, Anxa2(-/-) mice show increased NOD-like receptor family pyrin domain containing 3 (NLRP3) inflammasome activation in dendritic cells, elevated production of cytokines such as tumor necrosis factor-α (TNF-α), interleukin 6 (IL-6), interleukin-1β (IL-1β), and interferon-γ (IFN-γ), decreased macrophage-mediated bacterial clearance, excessive superoxide release, and increased pulmonary neutrophil infiltration.[22–24] Nuclear factor kappa-B (NF-κB), a dimeric transcription factor, further regulates key physiological processes, including inflammation, immunity, apoptosis, and the cell cycle.[25] When NF-κB signaling is initiated, phosphorylation of NF-κB p65 promotes its translocation into the nucleus, where it binds to specific DNA sequences and triggers the expression of proinflammatory mediators. This process drives the release of cytokines such as TNF-α, IL-1β, and IL-6, thereby promoting the recruitment and accumulation of inflammatory cells.[26,27] In the complex pathological context of neural injury, critical inflammatory signaling pathways, including Anxa2/NF-κB are prone to dysregulation.[28] Evidence indicates that Anxa2, when stimulated by damage-associated signals, can directly interact with components of the inhibitor of κB kinase (IKK) complex to trigger NF-κB phosphorylation and subsequent nuclear translocation.[29] However, the altered intracellular environment following neural injury may compromise Anxa2's ability to precisely modulate NF-κB activity. Conversely, excessive or prolonged NF-κB activation can further disrupt Anxa2 expression and function, undermining regulatory feedback. This maladaptive interplay exacerbates neuroinflammation, diminishes neuronal survival, and impedes neural repair.[30] Although nanomedicines hold promise for targeted delivery, their nanoscale properties and neuroprotective mechanisms remain poorly understood. In this study, we report that PFCDs mitigate CIRI by exerting anti-neuroinflammatory effects via the Anxa2/NF-kB signaling pathway.

# Materials and Methods

## Reagents

Pearls were obtained from Inner Mongolia International Mongolian Medical Hospital (China). Urethane and Nimodipine were purchased from Aladdin Co. Ltd (China). Penicillin/streptomycin, cell counting kit-8 (CCK-8) solution, 1% trichlorotrityl tetrazolium chloride (TTC) staining solution, radio immunoprecipitation assay (RIPA) lysis buffer, bicinchoninic acid (BCA) assay kit, immunofluorescence blocking buffer, cyanine 3 (Cy3) immunofluorescence staining kit, 4% paraformaldehyde, and hematoxylin and eosin (H&E) staining kit were sourced from Beyotime Co. Ltd (China). Fetal bovine serum (FBS) was purchased from Gibco Co. Ltd (China). Roswell park memorial institute (RPMI)-1640 medium, 5x sample buffer, phosphate-buffered saline (PBS), and Triton X-100 were obtained from Servicebio Co. Ltd (China). Nylon filament was purchased from Cinontech Co. Ltd (China). Primary antibodies including anti-Anxa2, anti-NF-κB p65, anti-p-NF-κB p65, anti-GAPDH, and fluorescent secondary antibodies were purchased from Cell Signaling Technology Co. Ltd (USA), while anti-p-Anxa2 was purchased from Affinity Co. Ltd (China). Polyvinylidene fluoride membrane (PVDF) membranes were obtained from Millipore Co. Ltd (USA). TNF-α, IL-6, and IL-1β enzyme-linked immunosorbent assay (ELISA) Kits were acquired from Byabscience Biotechnology Co. Ltd (China).

## Cell Lines and Animals

Rat adrenal pheochromocytoma (PC12) cells were sourced from Beyotime Co. Ltd (China) and cultured in RPMI-1640 medium supplemented with 10% FBS and 1% penicillin/streptomycin. Culture conditions consisted of 37°C in a 5% $CO_2$ in a humidified incubator. Male Sprague-Dawley (SD) rats were purchased from the Liaoning Provincial Laboratory Animal Center (China) and kept in an SPF-grade barrier facility at 22–25°C with 55–60% relative humidity under a 12-hour light/dark cycle. Experimental procedures were performed following National Institutes of Health standards and approved by the Ethics Committee of Inner Mongolia Minzu University for Nationalities (Approval No. NM-LL-2025-07-23-01).

## Preparation and Characterization of Pearl Powder Fluorescent Carbon Dots

Pearls were ground and passed through a 200-mesh screen to obtain pearl powder. Next, 10g of pearl powder were added to a round-bottom flask containing simulated human gastric fluid (0.2g NaCl, 0.32g pepsin, 0.7mL concentrated hydrochloric acid, brought to 100mL with double-distilled water, pH ~ 1.2). The mixture was refluxed in an oil bath at 37°C with magnetic stirring for 24 hours, before being centrifuged at 12,000 rpm for 30 minutes to extract unreacted materials. The resulting yellow supernatant was obtained and transferred into a dialysis bag for dialysis against ultrapure water over three days, with regular water changes, until the pH approached neutral. The dialyzed yellow solution was then further purified by two consecutive centrifugations at 15,000 rpm for 30 minutes, and the supernatant was collected after centrifugation. The sample was microwaved at 50 Hz for 5 minutes and subsequently freeze-dried. The lyophilized PFCDs were resuspended in ultrapure water, sonicated for 1 minute, and, after confirming fluorescence and other properties using a fluorescence detector, recovered and stored at 4°C.

The PFCDs were characterized using various techniques commissioned from Beijing Yandog Technology Co. Ltd, including Dynamic Light Scattering (DLS; No. 250327162171), Zeta Potential measurement (No. 2503271654211), Transmission Electron Microscopy (TEM; No. 250516176340), Atomic Force Microscopy (AFM; No. 250401101861), Fluorescence Spectroscopy (FLS; No. 250401093246), X-ray Photoelectron Spectroscopy (XPS; No. 250625155843), and Fourier Transform Infrared Spectroscopy (FTIR; No. 250625140894).

## Characterization of Pearl Powder Fluorescent Carbon Dots Stability

To assess the stability and dispersibility of PFCDs, they were dispersed at a concentration of 1 mg/mL in deionized water, PBS, and RPMI-1640 medium. The dispersions were visually monitored over time to determine stability. On day 5, the morphology and aggregation state of PFCDs in the aqueous dispersion were examined by TEM to evaluate their colloidal stability.

## Cellular Uptake of Pearl Powder Fluorescent Carbon Dots

PC12 cells were seeded in 6-well plates at a density of $5\times10^4$ cells per well and incubated with RPMI-1640 medium containing PFCDs (100 μg/mL). After 6 hours, the cells were washed three times with PBS, fixed with 4% paraformaldehyde for 30 minutes, and permeabilized with 0.1% Triton X-100 for 10 minutes. The samples were then blocked with immunofluorescence blocking buffer for 1 hour and counterstained with DAPI for 10 minutes. Cellular uptake of PFCDs was visualized by their intrinsic fluorescence using a laser confocal microscope (Nikon, Japan) in the DiO channel (excitation: 484 nm; emission: 500–550 nm).

## Proliferation Experiment

PC12 cells were seeded in 96-well plates at a density of $5 \times 10^3$ cells/mL and cultured for 12 hours. Each well was treated with 100 μL of PFCDs at varying concentrations and incubated at 37°C for 24 hours. Following treatment, 10 μL of CCK-8 reagent was added to each well, and the plates were incubated at 37°C for 2 hours in dark conditions. Absorbance at 450 nm was measured using a microplate reader (Tecan SPARK, Switzerland).

Cell viability was calculated using the formula:

$$Cell\ viability\,(\%) = \frac{OD_{sample}}{OD_{control}} \times 100\%$$

where $OD_{sample}$ is the absorbance of the treated cells and $OD_{control}$ is the absorbance of the control group.

## Oxygen-Glucose Deprivation/Reoxygenation Model Constructs and Cell Viability Assays

PC12 cells were seeded in 96-well plates at a density of $5 \times 10^3$ cells/mL and cultured for 12 hours. To induce the OGD/R model, cells were washed and incubated in glucose-free RPMI-1640 medium, then subjected to hypoxia in a chamber containing 95% $N_2$, 5% $CO_2$, and 1% $O_2$ at 37 °C for 2 hours. The cells were subsequently returned to normoxic conditions and cultured in complete medium containing glucose for 24 hours of reoxygenation. Following this, 100 μL of

PFCDs at varying concentrations were added to the cells for 6, 12, or 24 hours. To each well, 10 μL of CCK-8 reagent was added, followed by incubation at 37 °C for 2 hours in dark conditions. Absorbance at 450 nm was measured, and the optimal PFCD concentration and treatment duration determined from these results were used for subsequent mechanistic experiments.

The cells were categorized into three groups: Control group, whereby PC12 cells were maintained in complete medium; OGD/R group, whereby the OGD/R model was induced as described previously; and PFCDs group, in which OGD/R-treated PC12 cells were exposed to 10 μg/mL PFCDs for 24 hours.

## Tandem Mass Tag Proteomics Assay

Tandem Mass Tag (TMT)-based quantitative proteomics was conducted by Shanghai BIOTREE Biomedical Science and Technology Co. Ltd (No. BQ-ZXF20201119). Gene Ontology (GO) annotations, including biological processes (BP), cellular component (CC), and molecular function (MF), were obtained from the GO database (https://www.geneontology.org). Kyoto Encyclopedia of Genes and Genomes (KEGG) pathway enrichment analysis was carried out using the KEGG database (https://www.kegg.jp/kegg/pathway.html). Protein-protein interaction (PPI) networks of differentially expressed proteins in key pathways were constructed using the STRING database (https://string-db.org) and visualized with Cytoscape v3.9.1.

## Construction of the Middle Cerebral Artery Occlusion/Reperfusion Model

Forty male SD rats (7–8 weeks old, 240–260 g) were acclimatized for one week and then randomly assigned to five groups (n = 8): Sham, MCAO/R, Nimodipine, PFCDs-24h, and PFCDs-72h. Anesthesia was induced via intraperitoneal injection of 20% urethane (5 mL/kg). The MCAO/R model was achieved using the Zea-Longa filament occlusion method.[31] The right common carotid artery (CCA), external carotid artery (ECA), and internal carotid artery (ICA) were exposed and carefully isolated. A nylon filament (0.34 mm in diameter) was inserted through a minor incision in the CCA and advanced into the ICA (18–20 mm from the bifurcation) to achieve right middle cerebral artery occlusion. After 1.5 hours of ischemia, the nylon filament was withdrawn by approximately 1 cm to initiate reperfusion. In the Sham group, only the CCA was exposed without nylon filament insertion or occlusion, while the MCAO/R procedure was performed in all other groups.

Rats in the Sham and MCAO/R groups received equal volumes of physiological saline by intravenous injection once daily for three consecutive days, starting after modeling. The Nimodipine group was treated with Nimodipine (1 mg/kg) by intragastric administration once daily for three days, starting after modeling. Rats in the PFCDs-24h group were given a single intravenous dose of PFCDs (1 mg/mL) after modeling, whereas rats in the PFCDs-72h group received intravenous injections of PFCDs (1 mg/mL) once daily for three consecutive days, starting after modeling.

## In vivo Brain Tracing of Pearl Powder Fluorescence Carbon Dots

To trace the distribution of PFCDs in brain tissue, Sham and MCAO/R rats were intravenously injected with PFCDs dissolved in physiological saline (1 mg/mL). At 24 hours post-injection, the rats underwent cardiac perfusion for fixation, after which the brain tissues were harvested. The brain tissues were fixed in 4% paraformaldehyde for 24 hours, followed by dehydration, clearing, and paraffin embedding. Tissue sections were subsequently prepared, rehydrated, and permeabilized with 0.5% Triton X-100 for 10 minutes. After blocking with immunofluorescence blocking buffer for 1 hour and nuclear staining with DAPI for 10 minutes, the sections were mounted and imaged using a laser confocal microscope in the DiO channel (excitation: 484 nm; emission: 500–550 nm) to detect the intrinsic fluorescence of PFCDs in rat brain tissue.

## Neurological Function Score

Neurological function was evaluated at 2 hours after CIRI (baseline, pre-treatment) and again at 72 hours after reperfusion (post-treatment) using Bederson's scoring system.[32] Grade 0 (0 points): no neurological deficits; Grade I (1 point): occasional flexion and adduction of the contralateral limb when lifted by the tail; Grade II (2 points): reduced resistance to lateral push accompanied by Grade I symptoms; Grade III (3 points): spontaneous circling toward the paralyzed side during free movement with Grade II signs; Grade IV (4 points): unconsciousness and inability to walk. Rats with scores of 1–3 at the 2-hour baseline assessment were excluded from further analysis.

## Trichlorotrityl Tetrazolium Chloride Staining

After drug intervention, animals were euthanized by decapitation under deep anesthesia, and brain tissue was collected, excluding the cerebellum, olfactory bulb, and lower brainstem. The tissue was briefly frozen at −20°C for 30 minutes and then sectioned into coronal slices of 2 mm thickness. The slices were incubated in 1% TTC solution at 37°C in the dark for 30 minutes, with the sections turned every 5 minutes to ensure uniform staining. After staining, the tissue samples were fixed in 4% paraformaldehyde overnight and then imaged the following day. Infarcted regions, identified as pale unstained areas, were quantified in each slice using ImageJ software, and total infarct volume was determined.

## Hematoxylin and Eosin Staining

Under anesthesia, rats underwent transcardial perfusion with 4% paraformaldehyde. Brain tissue was dissected, further fixed, rinsed, dehydrated, and embedded in paraffin. Coronal sections (3μm thick) posterior to the optic chiasm were prepared, dewaxed in xylene and ethanol, and stained using a H&E kit. After dehydration, the sections were coverslipped with neutral resin and examined under a microscope (Nikon, Japan), to assess cortical neuron morphology.

## Western Blot Assay

Cells and brain tissue were homogenized in RIPA lysis buffer, and protein concentrations were determined with a BCA assay kit. Protein samples were combined with 5x sample buffer at a 4:1 ratio, boiled at 95°C for 10 minutes, and separated by SDS-PAGE. Proteins were transferred onto 0.45μm PVDF membranes using the wet transfer technique. Membranes were blocked with 5% skim milk for 1 hour at room temperature, followed by overnight incubation at 4°C with primary antibodies: anti-Anxa2 (1:1000), anti-p-Anxa2 (1:500), anti-NF-κB p65 (1:1000), and anti-p-NF-κB p65 (1:1000). Following primary incubation, membranes were incubated with fluorescent secondary antibodies (1:1000) for 1 hour at room temperature. Protein expression was visualized using the Odyssey imaging system (LI-COR Biosciences, USA) and quantified with ImageJ software.

## Immunofluorescence Staining

Cells and brain tissue section samples were permeabilized with 0.5% Triton X-100 for 10 minutes and subsequently incubated in immunofluorescence blocking buffer for 1 hour. The samples then underwent overnight incubation at 4 °C with primary antibodies: anti-Anxa2 (1:100), anti-p-Anxa2 (1:50), anti-NF-κB p65 (1:100), and anti-p-NF-κB p65 (1:100). Next, samples were exposed to a Cy3-conjugated secondary antibody (1:1000) for 1 hour at room temperature and counterstained with DAPI for 10 minutes. Fluorescence images were captured with a laser confocal microscope, and ImageJ software was used to quantify average fluorescence intensity and positive cell counts.

## Enzyme-Linked Immunosorbent Assay

TNF-α, IL-6, and IL-1β levels in cell culture supernatants and rat serum were measured through ELISA, following the manufacturer's instructions.

## Statistical Analysis

Data are presented as mean ± standard deviation. One-way analysis of variance (ANOVA) enabled the comparison of continuous variables among groups, while categorical data were analyzed using chi-square tests. A P-value $< 0.05$ was considered statistically significant, and $P < 0.01$ was considered highly significant. SPSS 25.0 and GraphPad Prism 8.0.2 were utilized for statistical analyses.

# Results and Discussion

## Physical and Optical Properties of Pearl Powder Fluorescent Carbon Dots

Three independent measurements of PFCDs using DLS and Zeta potential revealed an average hydrodynamic size of 2.75 ± 1.74 nm and a Zeta potential of −18.8 ± 0.65 mV (Figure 1A). AFM analysis was used to characterize the surface morphology and size of the PFCDs. The results showed that the particles consistently had heights below 5 nm, with a root mean square roughness (Rq) of 0.474 nm and an average roughness (Ra) of 0.370 nm (Figure 1B). TEM images

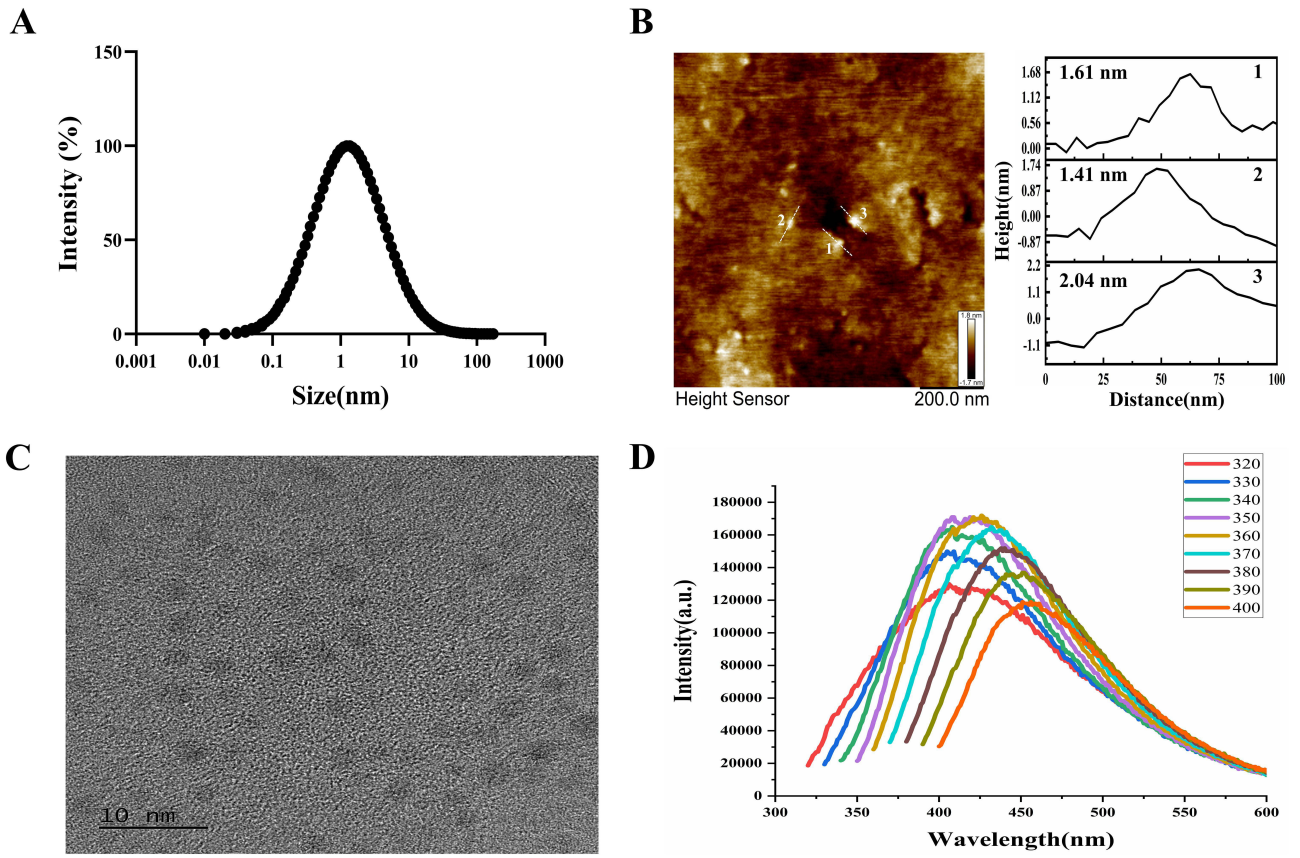


**Figure 1** (**A**) Average particle size and size distribution of PFCDs measured by DLS. (**B**) AFM 2D height map of PFCDs, with line profiles (white lines) of three representative particles used to determine particle height (scale bar: 200 nm). (**C**) Representative TEM image of PFCDs (scale bar: 10 nm). (**D**) FLS spectrum of PFCDs.

confirmed that PFCDs were quasi-spherical carbon nanoparticles (~5 nm diameter) with an equal size distribution (Figure 1C). FLS revealed considerable emission wavelength dependence. As the emission wavelength shifted from 320 nm to 400 nm, the central excitation peak of PFCDs red-shifted by over 48 nm (from 408 nm to >456 nm), accompanied by a >37.5% decrease in fluorescence intensity. This behavior suggests reduced electron-phonon coupling and an increasing contribution of non-radiative relaxation pathways. The observed red-shift and intensity decay were attributed to surface functional groups (–OH, –COOH, $–NH_2$), which introduce multiple excitation channels (n→π, π→π, and surface states) within the $sp^2$-hybridized carbon core. Combined with nanoscale effects, these groups create a continuous energy level gradient, leading to systematic excitation peak shifts and concurrent emission intensity reduction. Additionally, the full width at half maximum (FWHM) of the excitation band broadened from 42 nm to 55 nm, indicating energy level broadening due to surface defect states and enhanced non-radiative recombination (Figure 1D).

## Structural and Compositional Analysis of Pearl Powder Fluorescent Carbon Dots

XPS analysis was conducted to investigate the surface chemical composition and elemental valence states of PFCDs. The survey spectrum revealed that the main surface elements were C, O, N, Ca, Na, Cl, and Si, with C (64.03%) and O (24.87%) being the most abundant (Figure 2A and Table 1). High-resolution C 1s spectra showed four deconvoluted peaks: 284.84 eV, corresponding to C-C/C-H bonds that form the carbon backbone (43.16%); 286.30 eV, assigned to C-O or C-N bonds, indicative of hydroxyl, ether, or amine groups (32.39%); 288.13 eV, attributed to O-C=O structures such as carboxyl or ester groups (24.45%); and 289.40 eV, associated with C=N bonds (2.76%). These results confirm that PFCDs are enriched with organic substances, especially oxygen-containing functional groups, which contribute to their excellent biocompatibility and water dispersibility (Figure 2B). High-resolution Ca 2p analysis further revealed that calcium was present in the $Ca^{2+}$ state, represented by two symmetric peaks, Ca $2p_{3/2}$ (347.43 eV) and Ca $2p_{1/2}$ (350.97 eV), which are consistent with the


https://doi.org/10.2147/IJN.S567974

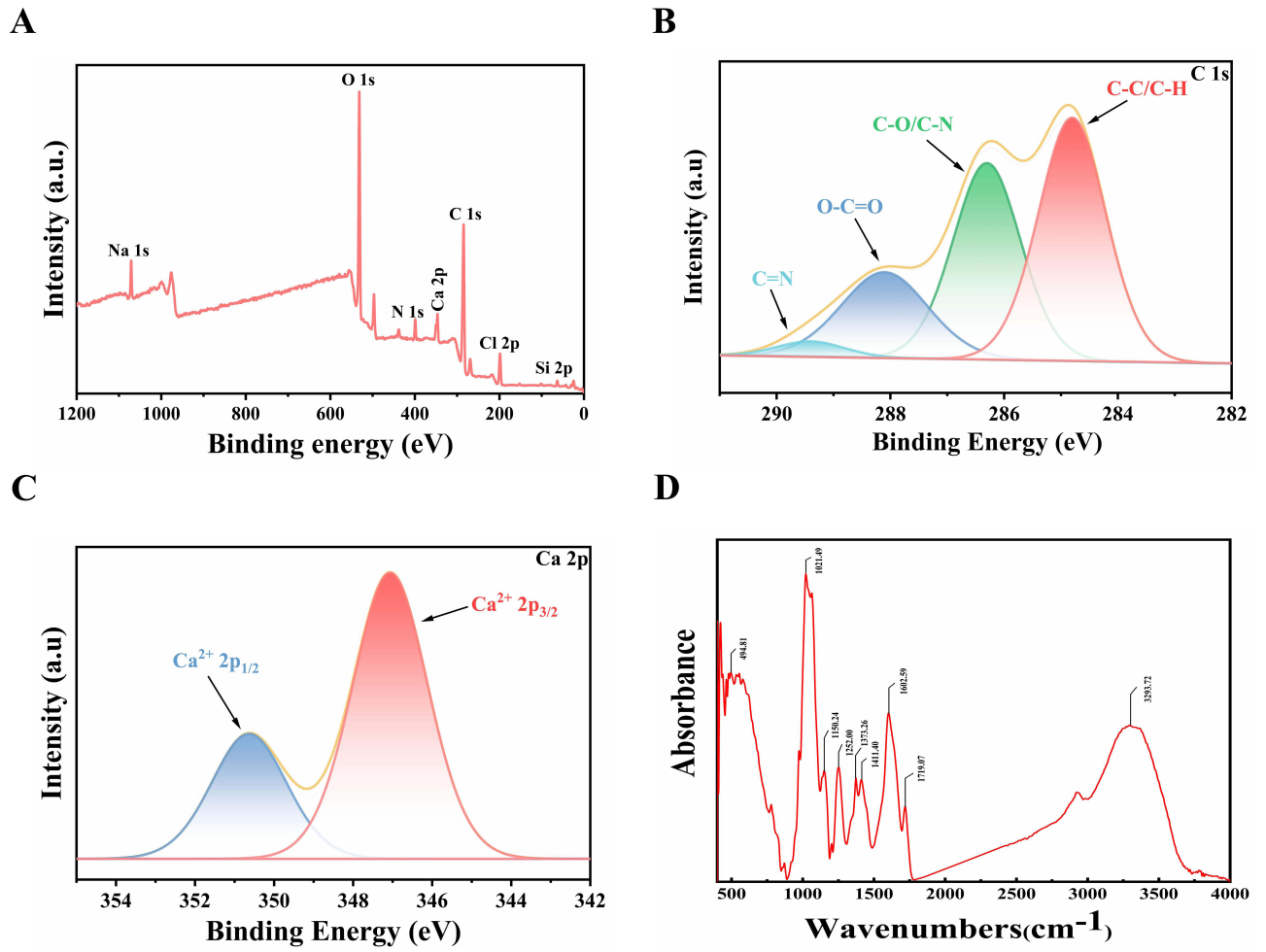


**Figure 2** (**A**) Survey XPS spectrum of PFCDs. (**B**) XPS C 1s spectrum of PFCDs. (**C**) XPS Ca 2p spectrum of PFCDs. (**D**) FTIR spectrum of PFCDs, presenting characteristic functional groups.

structural characteristics of calcium salts or calcium carbonate. Since strong satellite peaks typically accompany the Ca 2p peak of calcium carbonate but were absent in this spectrum, calcium was identified as primarily existing in the form of calcium phosphate. This finding implies that PFCDs contain calcium in a stable inorganic form (Figure 2C).

To complement the XPS analysis, FTIR spectroscopy was performed to further investigate the functional group composition of PFCDs. The FTIR spectrum (4000–400 $cm^{-1}$) exhibited characteristic absorption peaks consistent with

**Table 1** X-Ray Photoelectron Spectroscopy (XPS) Spectra of the PFCDs

| Name | Peak BE[a] | FWHM[b] | RSF[c] | Atomic Conc [%][d] |
|---|---|---|---|---|
| C 1s | 284.27 | 4.17 | 0.28 | 64.03 |
| O 1s | 531.27 | 3.18 | 0.78 | 24.87 |
| Cl 2p | 198.27 | 3.69 | 0.89 | 3.88 |
| N 1s | 399.27 | 2.68 | 0.48 | 3.35 |
| Ca 2p | 346.27 | 5.35 | 1.83 | 1.80 |
| Na 1s | 1071.27 | 2.61 | 1.69 | 1.55 |
| Si 2p | 100.27 | 3.91 | 0.33 | 0.50 |

**Notes**: [a]Peak BE refers to the energy loss of photoelectrons. [b]FWHM refers to the half-width of the spectral peak. [c]RSF refers to the relative sensitivity factor. [d]Atomic conc [%] refers to the atomic concentration percentage of the element.


https://doi.org/10.2147/IJN.S567974

the XPS results. A prominent absorption band at 3293 $cm^{-1}$ corresponded to O-H stretching vibrations associated with surface hydroxyl groups and adsorbed water. The peak at 1719 $cm^{-1}$ was assigned to C=O stretching of carboxyl groups (-COOH). The absorption at 1602 $cm^{-1}$ was assigned to N-H bending (amide groups) and/or aromatic C=C stretching, indicating the presence of nitrogen-containing organic components. A band at 1411 $cm^{-1}$ was attributed to the symmetric stretching of $COO^-$ groups, while the peak at 1252 $cm^{-1}$ was primarily associated with P=O stretching of phosphate moieties. Additional peaks at 1150 $cm^{-1}$ and 1021 $cm^{-1}$ aligned with C-O-C and C-O stretching vibrations, respectively. Finally, a band at 495 $cm^{-1}$ was attributed to P-O bending modes within the calcium phosphate framework (Figure 2D).

In summary, FTIR analysis confirmed that PFCDs exhibit an organic–inorganic hybrid structure. The organic fraction is enriched with hydroxyl, carboxyl, and amine/amide functional groups, which enhance hydrophilicity and align with the carbon, oxygen, and nitrogen elements detected by XPS. Together with the presence of calcium phosphate, these findings verify that PFCDs represent a typical organic–inorganic composite system. Such a structure not only supports good biocompatibility but also offers multiple reactive sites for further functionalization.

## Stability Characterization of Pearl Powder Fluorescence Carbon Dots

PFCDs remained uniformly dispersed in all tested media, with no visible precipitation or aggregation observed. After 5 days of storage, the PFCD dispersion in deionized water was further analyzed by TEM, revealing a homogeneous particle size distribution with no significant aggregation or morphological alterations (Figure S1). These results demonstrate that PFCDs possess excellent dispersibility and formulation stability under in vitro conditions, which is essential for maintaining consistent physicochemical properties in subsequent biological studies.

## Cellular Uptake of Pearl Powder Fluorescence Carbon Dots

To evaluate the internalization of PFCDs by neuronal cells, cellular uptake was assessed using PC12 cells. After 6 hours of co-incubation with PFCDs, a notable increase in green fluorescence was observed in the PFCD-treated group compared with the control group (Figure S2). This result indicates that PFCDs were effectively internalized by PC12 cells and exhibited stable intracellular fluorescence, supporting their biocompatibility and suitability for cellular tracking applications.

## Pearl Powder Fluorescent Carbon Dots Enhance Cell Viability in Oxygen-Glucose Deprivation/Reoxygenation-Injured PC12 Cells

The impact of different concentrations on PFCDs on the viability of PC12 cells was determined with a CCK-8 assay. Treatment with 100 μg/mL PFCDs over a 24-hour period produced the highest cell viability relative to the control (Figure 3A), and concentrations up to 100 μg/mL were therefore selected for further experiments. To evaluate the neuroprotective outcome of PFCDs against OGD/R-induced injury, cells underwent OGD/R treatment and subsequently treated with PFCDs (10–-100 μg/mL) for 6, 12, or 24 hours. OGD/R significantly reduced cell viability compared to the control (Figure 3B and C). However, after 24 hours of treatment, 10 μg/mL PFCDs significantly increased viability relative to the OGD/R group, resulting in an IC50 of 13.32 μg/mL (Figure 3D). Based on these results, 10 μg/mL PFCDs and a 24-hour treatment period were chosen as the optimal conditions for subsequent mechanistic studies.

## Proteomic Profiling Reveals NF-κB Signaling Pathway Modulation by Pearl Powder Fluorescent Carbon Dots

Proteomic analysis identified 7535 proteins in PC12 cells following OGD/R treatment. Differentially expressed proteins were clustered using hierarchical clustering and visualized as a heatmap, with the criteria set as unique peptides ≥ 1, fold change > 1.2, and $P < 0.05$ (Student's *t*-test or one-way ANOVA). The resulting differentially expressed proteins effectively distinguished between the comparison groups, validating the screening approach (Figure 4A–C). Key proteins and subnetworks among the differentially expressed proteins in the Control vs OGD/R, Control vs PFCDs, and OGD/R vs PFCDs comparisons were further identified using the Network Analyzer function in Cytoscape, and the corresponding reciprocal interaction networks were constructed (Figure 4D–F).

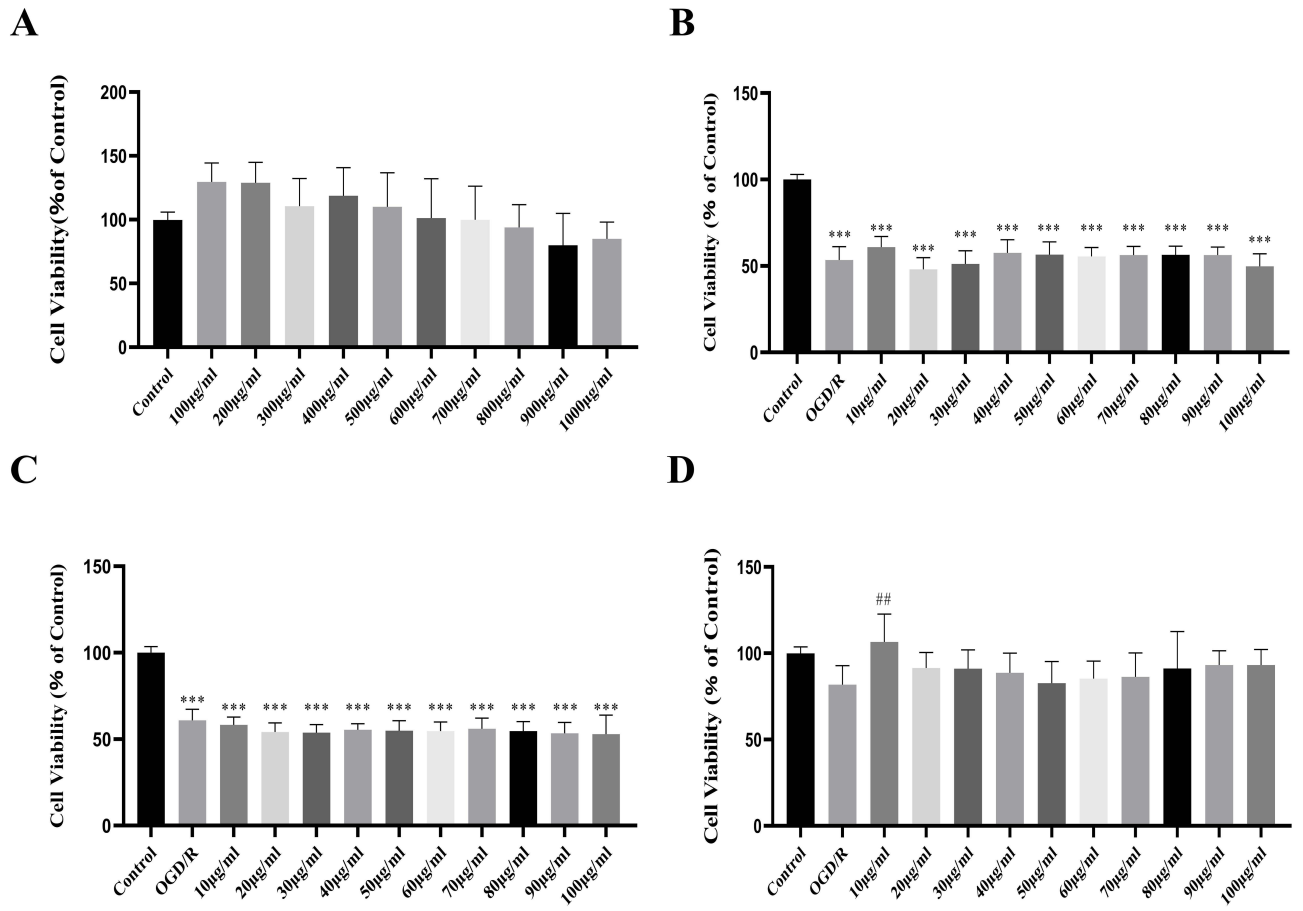


**Figure 3** (**A**) Viability of PC12 cells after 24 hour treatment with PFCDs (100–1000 μg/mL) (mean ± SD, n=6). (**B**–**D**) Viability of OGD/R-induced PC12 cells following PFCD treatment (10–100 μg/mL) for 6, 12, and 24 hours (mean ± SD, n=6). Statistical significance: ***P < 0.001 vs Control group; ##P < 0.01 vs OGD/R group.

KEGG pathway enrichment analysis using Fisher's exact test revealed significant alterations in metabolic and signaling pathways across the experimental groups. In the Control vs OGD/R comparison, key pathways including amino sugar and nucleotide sugar metabolism, glycolysis/gluconeogenesis, starch and sucrose metabolism, cysteine and methionine metabolism, and terpenoid backbone biosynthesis were significantly affected (Figure 4G). For the Control vs PFCDs group, notable changes occurred in pathways including endocytosis, Salmonella infection, pyruvate metabolism, sphingolipid metabolism, and small cell lung cancer (Figure 4H). In the OGD/R vs PFCDs comparison, significant alterations were observed in pathways including mismatch repair, oxidative phosphorylation, non-alcoholic fatty liver disease, Huntington disease, nucleotide excision repair, thermogenesis, and NF-κB signaling pathway (Figure 4I).

GO functional enrichment analysis using Fisher's exact test identified significantly differentially expressed proteins across the experimental groups. In the Control vs OGD/R comparison, key biological processes included organic substance catabolic process, carbohydrate metabolic process, oxoacid metabolic process, organic acid metabolic process, and carboxylic acid metabolic process. Molecular functions such as protein homodimerization activity, transferase activity, lyase activity, farnesyltranstransferase activity, and hydrolase activity were significantly altered. Subcellular localization changes were observed in the cytoskeleton, Golgi apparatus, prefoldin complex, mitotic spindle, and cytoskeletal part (Figure 4J). For the Control vs PFCDs group, notable biological processes affected included cellular component biogenesis, cellular metabolic process, ribosome biogenesis, protein-containing complex subunit organization, and rRNA processing. Altered molecular functions included coenzyme binding, enzyme binding, protein-containing complex binding, and nucleoside-triphosphatase activity, while localization changes were detected in the organelle membrane, endomembrane system, nuclear part, and whole membrane (Figure 4K). In the OGD/R vs PFCDs group, significant biological processes included DNA replication, nucleotide metabolic process, generation of precursor metabolites and energy, oxidation-reduction processes, and electron transport chain. Molecular functions

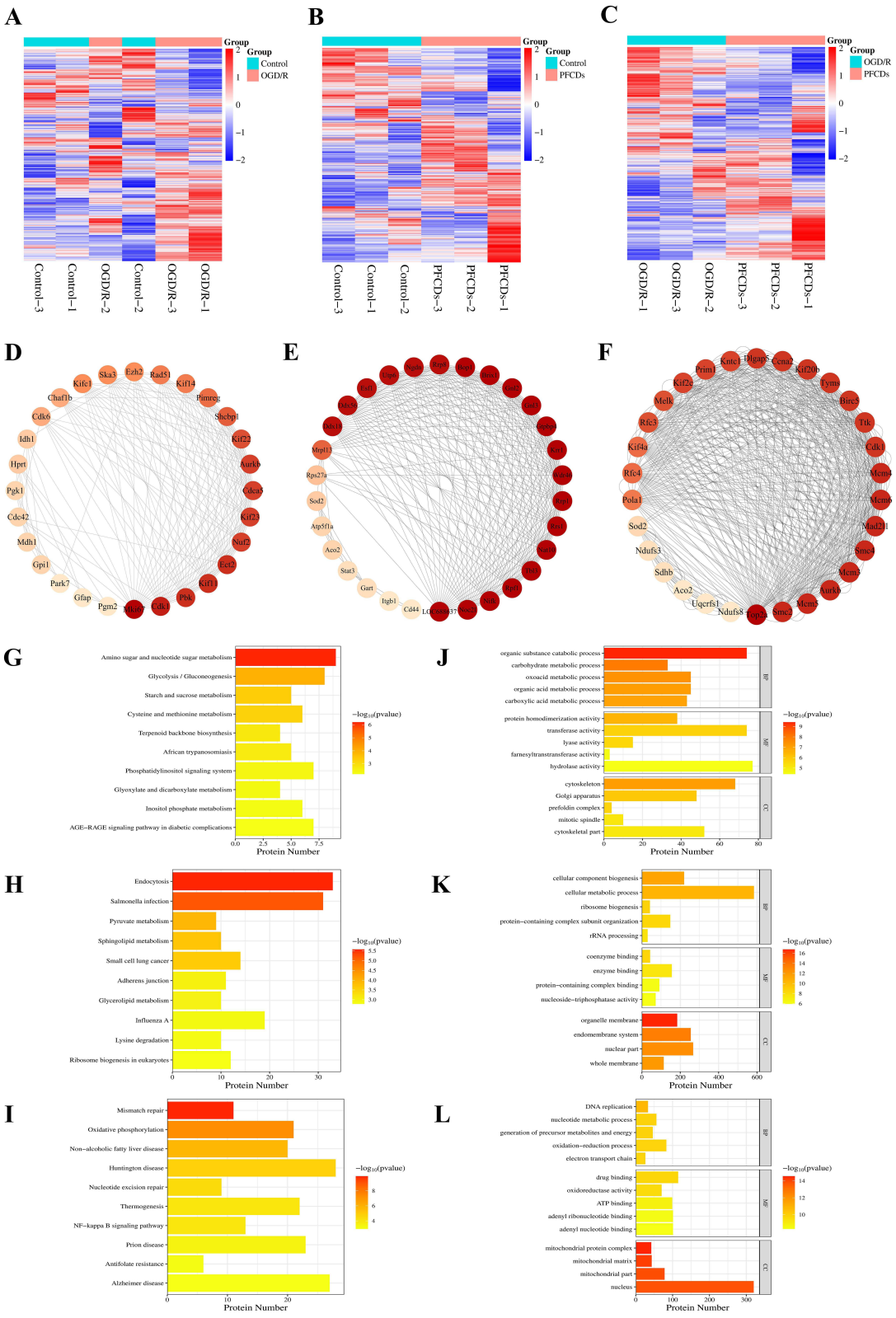


**Figure 4** Proteomic profiling and bioinformatic analysis of PC12 cells across experimental groups. (**A–C**) Hierarchical clustering heatmaps of differentially expressed proteins identified by proteomic analysis. Red and blue indicate significantly upregulated and downregulated proteins, respectively, while gray represents missing quantitative data. (**D–F**) PPI networks constructed from the differentially expressed proteins, with the top 30 proteins ranked by node degree highlighted for visualization. (**G–I**) KEGG pathway enrichment analysis, showing significantly enriched pathways on the y-axis and the number of differentially expressed proteins in each pathway on the x-axis. (**J–L**) GO functional enrichment analysis, with enriched terms grouped into biological process (BP), molecular function (MF), and cellular component (CC); the x-axis represents the number of differentially expressed proteins associated with each term. Panels in each column correspond to the following pairwise comparisons: (**A, D, G** and **J**) to Control vs OGD/R; (**B, E, H** and **K**) to Control vs PFCDs; (**C, F, I** and **L**) to OGD/R vs PFCDs.


https://doi.org/10.2147/IJN.S567974

such as drug binding, oxidoreductase activity, ATP binding, adenyl ribonucleotide binding, and adenyl nucleotide binding were affected, with subcellular localization changes observed in the mitochondrial protein complex, mitochondrial matrix, mitochondrial part, and nucleus (Figure 4L).

Proteomic analysis revealed that PFCDs treatment significantly restored the expression of NF-κB signaling pathway-related proteins disrupted by OGD/R. Supporting this, KEGG pathway enrichment analysis showed substantial modulation of the NF-κB signaling pathway. Together, these results indicate that the NF-κB signaling pathway is a primary target through which PFCDs exert their anti-neuroinflammatory effects.

## Pearl Powder Fluorescent Carbon Dots Suppress Anxa2/NF-κB Signaling Pathway Activation and Inflammatory Cytokine Release in vitro

To evaluate the inhibitory effect of PFCDs on Anxa2/NF-κB signaling pathway activation in vitro, PC12 cells were harvested and proteins were extracted for immunoblotting analysis of Anxa2, p-Anxa2, NF-κB p65, and p-NF-κB p65. OGD/R exposure strongly stimulated the Anxa2/NF-κB signaling pathway in PC12 cells, while PFCDs treatment effectively inhibited this activation. Relative to the control group, p-Anxa2 expression was significantly elevated in the OGD/R group but was significantly downregulated following PFCDs intervention. Similarly, p-NF-κB p65 levels were moderately increased in OGD/R-treated cells, and this increase was significantly diminished by PFCDs intervention (Figure 5A–C). Immunofluorescence staining for p-Anxa2 and p-NF-κB p65 corroborated these results. The OGD/R group exhibited markedly higher fluorescence intensities for both proteins relative to the control, whereas PFCDs treatment significantly reduced these signals (Figure 5D–G). Furthermore, ELISA assays demonstrated that OGD/R-injured PC12 cells exhibited markedly increased secretion of the pro-inflammatory cytokines TNF-α, IL-6, and IL-1β compared to controls. Treatment with PFCDs notably lowered the extracellular levels of these cytokines compared to the OGD/R group (Figure 5H–J).

Collectively, these in vitro results demonstrate that PFCDs effectively protect PC12 cells from OGD/R-induced inflammatory damage by specifically modulating the Anxa2/NF-κB signaling pathway. Both immunoblotting and immunofluorescence analyses consistently showed that PFCDs significantly inhibit OGD/R-induced phosphorylation of Anxa2 and NF-κB p65, key mediators of the pro-inflammatory cascade. This pathway suppression correspondingly resulted in a significant reduction in the secretion of major pro-inflammatory cytokines, including TNF-α, IL-6, and IL-1β.

## In vivo Brain Tracing of Pearl Powder Fluorescence Carbon Dots

To assess the ability of PFCDs to cross the BBB under pathological conditions, PFCDs were intravenously administered to Sham and MCAO/R rats. The MCAO/R+PFCDs group exhibited significantly stronger green fluorescence in the brain parenchyma, along with a markedly higher percentage of $DiO^{+}$ cells, compared with the Sham+PFCDs group (Figure S3A and B). Since ischemic brain injury is known to disrupt BBB integrity and increase its permeability,[33] the enhanced accumulation of PFCDs in the MCAO/R brains was attributed primarily to facilitated nanoparticle penetration across the compromised BBB. These findings suggest that PFCDs can efficiently access brain tissue under pathological conditions and enable fluorescence-based visualization and distribution tracing. This capability highlights the potential of PFCDs as diagnostic imaging probes or drug delivery carriers for brain-related diseases.

## Pearl Powder Fluorescence Carbon Dots Ameliorate Neuropathology in Middle Cerebral Artery Occlusion/Reperfusion Rats

The Sham group presented a Bederson score of 0, indicating normal neurological function with no observable deficits. Meanwhile, the MCAO/R group exhibited notably elevated neurological scores, reflecting impairments such as contralateral limb flexion/adduction, unilateral weakness, and circling behavior. All other experimental groups also showed higher scores than the Sham group at 2 hours post-cerebral ischemia-reperfusion (Figure 6A). At 72-hours post-treatment, both Nimodipine and PFCDs-72h interventions significantly reduced neurological scores compared to the MCAO/R group, indicating substantial mitigation of neurological deficits (Figure 6B). TTC staining revealed uniformly red brain sections in the Sham group, indicating absence of infarction, whereas the MCAO/R group displayed extensive white infarct regions. Treatment with Nimodipine or

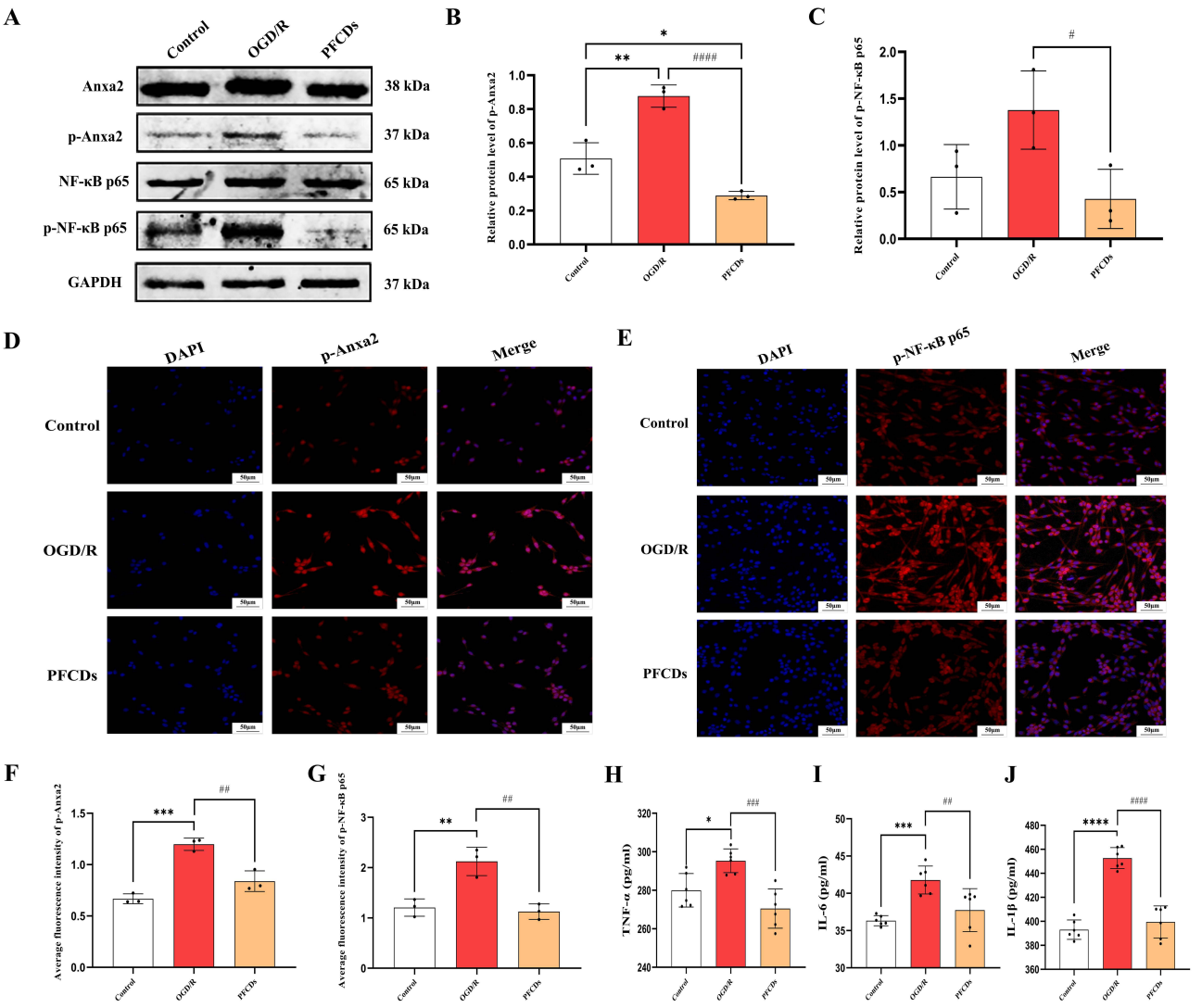


**Figure 5** (**A**) Representative immunoblot of Anxa2, p-Anxa2, NF-κB p65, and p-NF-κB p65 in PC12 cells across experimental groups. (**B** and **C**) Quantification of p-Anxa2 and p-NF-κB p65 protein levels in PC12 cells (mean ± SD, n=3). (**D** and **E**) Representative immunofluorescence images of p-Anxa2 and p-NF-κB p65 in PC12 cells, with nuclei stained by DAPI (scale bar: 50 μm). (**F** and **G**) Quantification of fluorescence intensity for p-Anxa2 and p-NF-κB p65 in PC12 cells (mean ± SD, n=3). (**H–J**) Extracellular levels of TNF-α, IL-6, and IL-1β in PC12 cells measured by ELISA (mean ± SD, n=6). Statistical significance: *P < 0.05, **P < 0.01, ***P < 0.001, ****P < 0.0001 vs Control group; #P < 0.05, ##P < 0.01, ###P < 0.001, ####P < 0.0001 vs OGD/R group.

PFCDs-72h markedly decreased infarct size relative to the MCAO/R group at 72 hours (Figure 6C and D). HE staining revealed regularly arranged neurons in the Sham group, with round morphologies, intact cellular structures, prominent nucleoli, and clearly defined boundaries. Conversely, neurons in the MCAO/R group showed severe degeneration, including tissue disorganization, interstitial edema, neuronal swelling with triangular or irregular shapes, nuclear pyknosis, and karyorrhexis. All drug-treated groups exhibited significant improvements in neuronal morphology compared to the MCAO/R group, indicating effective neuroprotection (Figure 6E).

## Pearl Powder Fluorescence Carbon Dots Suppress Anxa2/NF-κB Signaling Pathway Activation and Inflammatory Cytokine Release in vivo

To confirm the inhibitory impact of PFCDs on the Anxa2/NF-κB signaling pathway in MCAO/R rat brains, cortical proteins were analyzed by immunoblotting for Anxa2, p-Anxa2, NF-κB p65, and p-NF-κB p65. The outcome revealed activation of Anxa2/NF-κB signaling pathway following MCAO/R injury. In comparison to the Sham group, the MCAO/R group exhibited significant upregulation of Anxa2 and NF-κB p65 protein levels. Following treatment, both the Nimodipine and PFCDs-72h


https://doi.org/10.2147/IJN.S567974

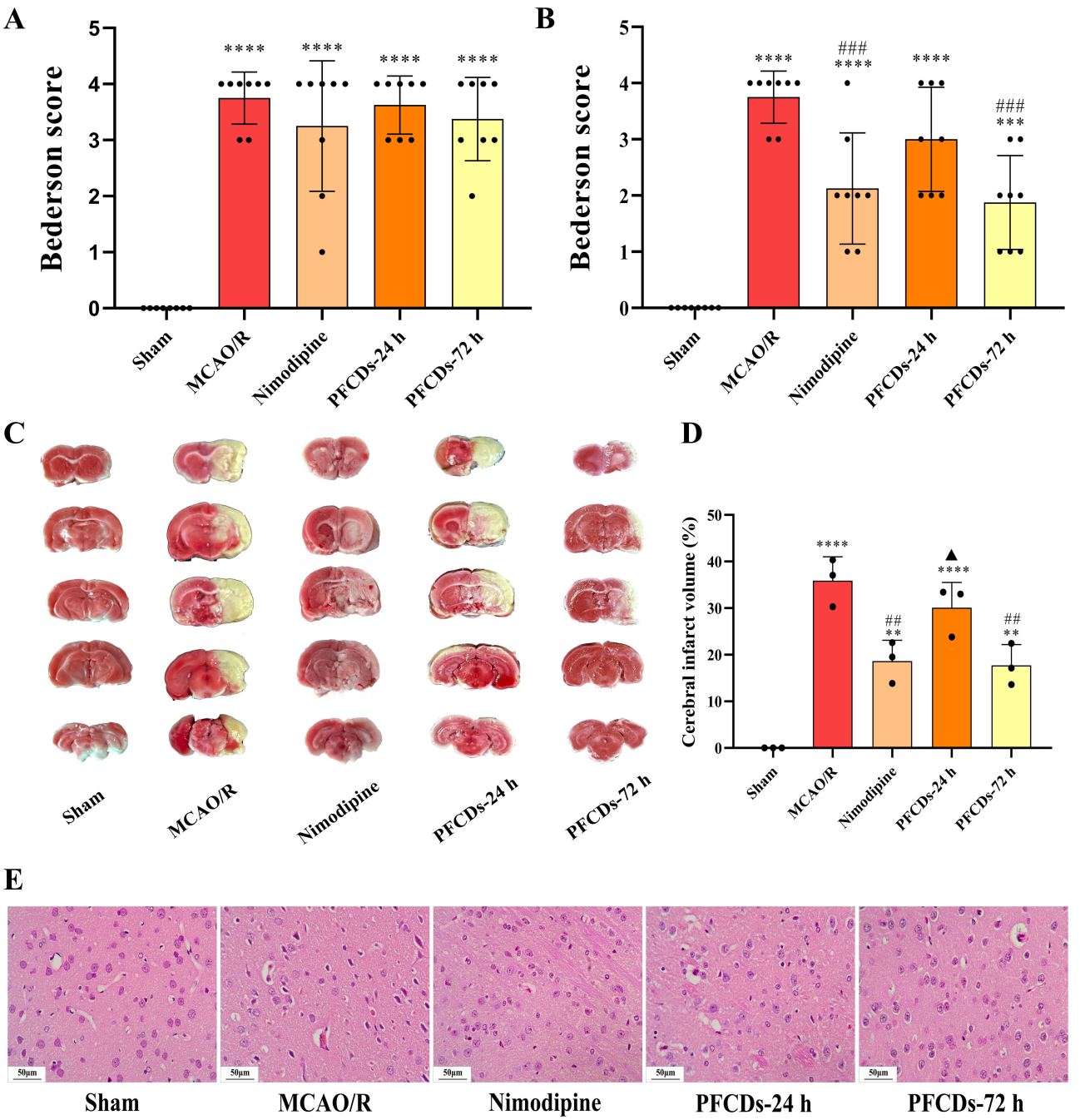


**Figure 6** (**A** and **B**) Bederson neurological scores of experimental rats measured 2 hours post-cerebral ischemia-reperfusion and 72 hours post-treatment (mean ± SD, n=8). (**C**) Representative TTC-stained brain sections showing cerebral infarction in experimental rats. (**D**) Percentage of cerebral infarction volume at 72 hours post-treatment (mean ± SD, n=3). (**E**) Representative Hematoxylin and Eosin-stained images of neuronal morphology in the peri-ischemic cortex (scale bar: 50 μm). Statistical significance: $^{**}P < 0.01$, $^{***}P < 0.001$, $^{****}P < 0.0001$ vs Sham group; $^{\#\#}P < 0.01$, $^{\#\#\#\#}P < 0.001$ vs MCAO/R group; $^{\blacktriangle}P < 0.05$ vs Nimodipine group.

groups showed downregulation of Anxa2 expression, while the PFCDs-24h and PFCDs-72h group also significantly reduced NF-κB p65 expression (Figure 7A–C). These findings were further supported by immunofluorescence staining of Anxa2 and NF-κB p65 in brain tissue. The MCAO/R group displayed a significantly higher percentage of $Anxa2^{+}$ and NF-κB $p65^{+}$ cells compared with the Sham group. Drug administration significantly reduced the percentage of $Anxa2^{+}$ cells in the Nimodipine, PFCDs-24h, and PFCDs-72h groups, whereas only the PFCDs-72h group significantly decreased the percentage of NF-κB $p65^{+}$ cells relative to the MCAO/R group (Figure 7D–G). Consistent with these results, ELISA analysis showed that the serum concentrations of the pro-inflammatory cytokines TNF-α, IL-6, and IL-1β were notably increased in the MCAO/R group

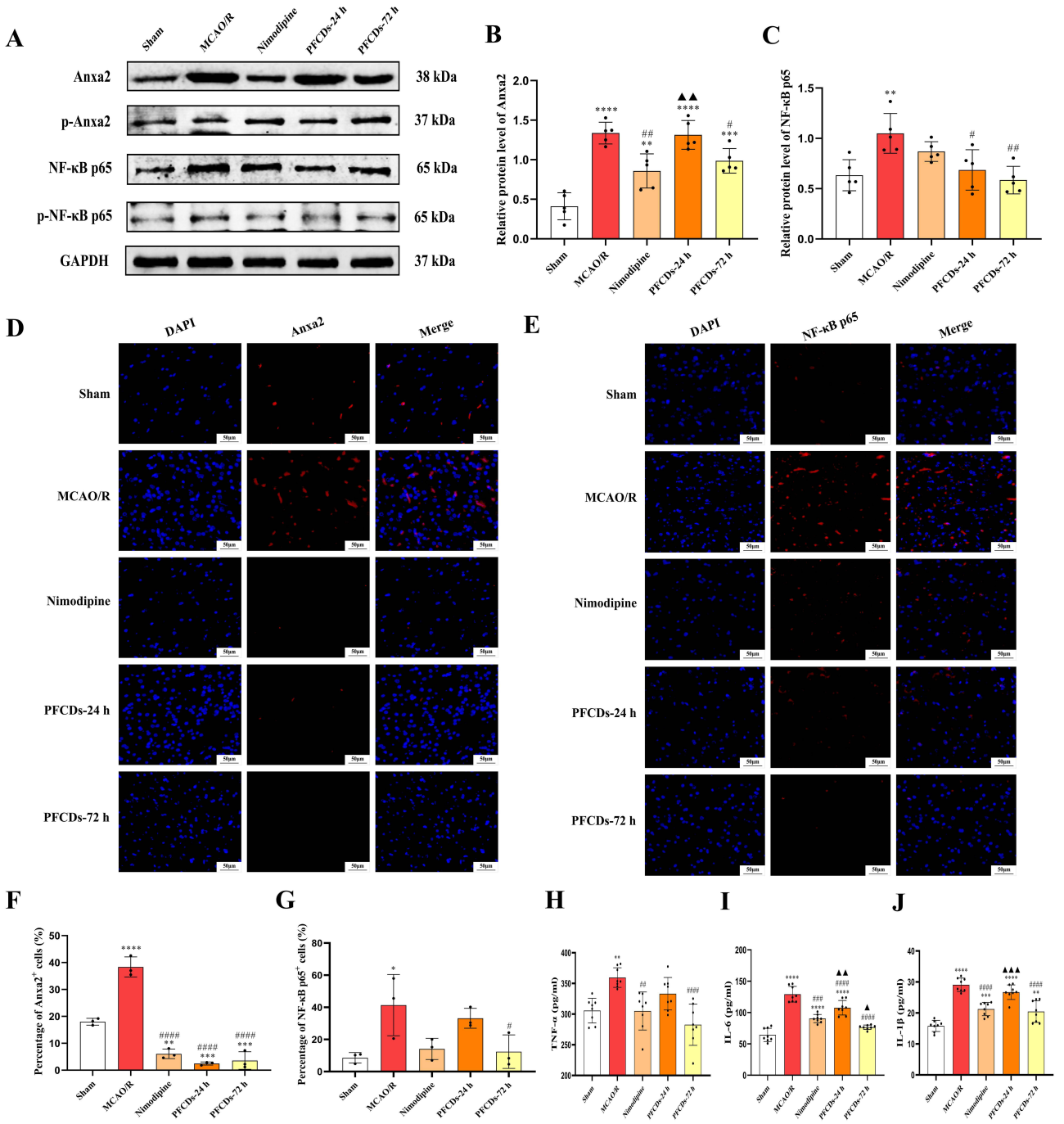


**Figure 7** (**A**) Representative immunoblots of Anxa2, p-Anxa2, NF-κB p65, and p-NF-κB p65 in brain tissue of experimental rats. (**B** and **C**) Quantification of Anxa2 and NF-κB p65 protein expression levels (mean ± SD, n=5). (**D** and **E**) Representative immunofluorescence images of Anxa2 and NF-κB p65 in brain tissue, with nuclei stained using DAPI (scale bar: 50 μm). (**F** and **G**) Percentage of $Anxa2^+$ cells and NF-κB $p65^+$ cells in brain tissue, expressed as a percentage of $DAPI^+$ cells (mean ± SD, n=3). (**H–J**) Serum levels of TNF-α, IL-6, and IL-1β measured by ELISA (mean ± SD, n=8). Statistical significance: *P < 0.05, **P < 0.01, ***P < 0.001, ****P < 0.0001 vs Sham group; $^{\#}$P < 0.05, $^{\#\#}$P < 0.01, $^{\#\#\#}$P < 0.001, $^{\#\#\#\#}$P < 0.0001 vs MCAO/R group. $^{\blacktriangle}$P < 0.05, $^{\blacktriangle\blacktriangle}$P < 0.01, $^{\blacktriangle\blacktriangle\blacktriangle}$P < 0.001 vs Nimodipine group.

relative to those in the Sham group. Treatment with Nimodipine or PFCDs-72h significantly decreased the levels of these cytokines compared to the MCAO/R group (Figure 7H–J).

This study provides the in vivo evidence that PFCDs mitigate neuroinflammation in MCAO/R rats by targeting the Anxa2/NF-κB signaling pathway. Western blot and immunofluorescence consistently demonstrated that total Anxa2 and NF-κB p65 levels were elevated in MCAO/R brain tissues, but were significantly reduced following 72 hours of PFCDs


https://doi.org/10.2147/IJN.S567974

treatment. Notably, the therapeutic efficacy of PFCDs-72h in downregulating Anxa2 and NF-κB p65 expression and lowering pro-inflammatory cytokines was comparable to that of Nimodipine, a clinically established neuroprotective drug, highlighting the considerable translational potential of PFCDs. Interestingly, unlike the clear changes in total protein expression, phosphorylation levels of Anxa2 and NF-κB p65 did not reach statistical significance in vivo. This discrepancy may reflect the complexity of the MCAO/R brain microenvironment, which comprises diverse cell types, including neurons, astrocytes, microglia, and infiltrating peripheral immune cells,[34] compared with the simplified conditions of in vitro cell models. Given that NF-κB signaling in cerebral ischemia is highly context- and cell type-dependent,[35] PFCDs may exert their protective effects not by directly suppressing phosphorylation of core proteins such as NF-κB p65, but rather by downregulating upstream regulators such as Anxa2 or indirectly modulating neuroinflammation through parallel signaling mechanisms. The observed reduction in total Anxa2 and NF-κB p65, together with decreased TNF-α, IL-6, and IL-1β levels, strongly supports the conclusion that PFCDs functionally inhibit Anxa2/NF-κB signaling pathway activity. Furthermore, the contrasting outcomes between single-dose (PFCDs-24h) and multi-dose (PFCDs-72h) regimens underscore the importance of treatment duration. Prolonged administration achieved stronger suppression of Anxa2/NF-κB signaling pathway and downstream inflammatory mediators. These findings emphasize that sustained inhibition of inflammatory signaling is critical for maximizing the therapeutic potential of PFCDs.

## Limitations and Future Directions

Despite the encouraging findings, this study has certain limitations that warrant attention. The biodistribution, metabolic kinetics, and BBB penetration efficiency of PFCDs were not quantified, yet these parameters are critical for optimizing clinical dosing strategies. In addition, the upstream regulatory mechanisms driving Anxa2 phosphorylation, such as calcium influx or oxidative stress, and their interactions with PFCDs remain poorly understood. To address these gaps, future studies will aim to design brain-targeted PFCD delivery systems through surface modification strategies, combined with real-time imaging tracers to track in vivo distribution. In parallel, multi-omics approaches will be applied to systematically dissect the upstream regulation of Anxa2/NF-κB signaling and clarify the interplay between PFCDs and neuroinflammatory pathways.

## Conclusions

This study introduces a novel approach for synthesizing PFCDs via enzymatic digestion. The resulting PFCDs possess ultra-small particle sizes, unique optical characteristics, high stability, and excellent biocompatibility. Structural analyses demonstrated that PFCDs possess a unique organic-inorganic hybrid architecture. The organic component consists predominantly of carbon, oxygen, and nitrogen, and is richly functionalized with hydrophilic groups including hydroxyl, carboxyl, and amine/amide moieties. This organic matrix is integrated with an inorganic phase dominated by calcium phosphate. Systematic evaluation using both in vitro OGD/R-induced PC12 cell injury models and in vivo MCAO/R rat models demonstrated that PFCDs significantly promoted cell viability, improved neurological function, reduced cerebral infarct volume, and alleviated neuronal morphological damage. Mechanistically, the anti-neuroinflammatory effects of PFCDs were attributed to their ability to suppress activation of the Anxa2/NF-κB signaling pathway, thus attenuating proinflammatory cytokine release.

## Abbreviations

PFCDs, pearl powder fluorescent carbon dots; CDs, carbon dots; IS, ischemic stroke; CIRI, cerebral ischemia/reperfusion; OGD/R, oxygen–glucose deprivation/reoxygenation; MCAO/R, middle cerebral artery occlusion/reperfusion; Anxa2, Annexin A2; NF-κB, nuclear factor kappa-B; TNF-α, tumor necrosis factor-α; IL-6, interleukin 6; IL-1β, interleukin-1β.

## Acknowledgments

This work was supported by the Education Department of Inner Mongolia Autonomous Region of China (NO. KC2024054B) and the National and Local Joint Mongolian Medicine R&D Engineering Center of China (NO. MDK2023039).

## Disclosure

The authors declare that they have no conflicts of interest in this work.

## References


1. Ospel JM, Nguyen TN, Jadhav AP, et al. Endovascular treatment of medium vessel occlusion stroke. *Stroke*. 2024;55(3):769–778. doi:10.1161/strokeaha.123.036942
2. Lim S, Kim TJ, Kim YJ, Kim C, Ko SB, Kim BS. Senolytic therapy for cerebral ischemia-reperfusion injury. *Int J Mol Sci*. 2021;22(21):11967. doi:10.3390/ijms222111967
3. Wang L, Zhang X, Xiong X, et al. Nrf2 regulates oxidative stress and its role in cerebral ischemic stroke. *Antioxidants*. 2022;11(12):2377. doi:10.3390/antiox11122377
4. Candelario-Jalil E, Dijkhuizen RM, Magnus T. Neuroinflammation, stroke, blood-brain barrier dysfunction, and imaging modalities. *Stroke*. 2022;53(5):1473–1486. doi:10.1161/strokeaha.122.036946
5. Yang C, Hawkins KE, Doré S, Candelario-Jalil E. Neuroinflammatory mechanisms of blood-brain barrier damage in ischemic stroke. *Am J Physiol Cell Physiol*. 2019;316(2):C135–C153. doi:10.1152/ajpcell.00136.2018
6. Wu L, Xiong X, Wu X, et al. Targeting oxidative stress and inflammation to prevent ischemia-reperfusion injury. *Front Mol Neurosci*. 2020;13:28. doi:10.3389/fnmol.2020.00028
7. He X, Wang X, Yang L, et al. Intelligent lesion blood-brain barrier targeting nano-missiles for Alzheimer's disease treatment by anti-neuroinflammation and neuroprotection. *Acta Pharm Sin B*. 2022;12(4):1987–1999. doi:10.1016/j.apsb.2022.02.001
8. Cheng Y, Cheng A, Jia Y, et al. pH-responsive multifunctional theranostic rapamycin-loaded nanoparticles for imaging and treatment of acute ischemic stroke. *ACS Appl Mater Interfaces*. 2021;13(48):56909–56922. doi:10.1021/acsami.1c16530
9. Luo WK, Zhang LL, Yang ZY, et al. Herbal medicine derived carbon dots: synthesis and applications in therapeutics, bioimaging and sensing. *J Nanobiotechnology*. 2021;19(1):320. doi:10.1186/s12951-021-01072-3
10. Wu T, Bai X, Zhang Y, et al. Natural medicines-derived carbon dots as novel oral antioxidant administration strategy for ulcerative colitis therapy. *J Nanobiotechnology*. 2024;22(1):511. doi:10.1186/s12951-024-02702-2
11. Li CL, Ou CM, Huang CC, et al. Carbon dots prepared from ginger exhibiting efficient inhibition of human hepatocellular carcinoma cells. *J Mater Chem B*. 2014;2(28):4564–4571. doi:10.1039/c4tb00216d
12. Wang J, Wang CF, Chen S. Amphiphilic egg-derived carbon dots: rapid plasma fabrication, pyrolysis process, and multicolor printing patterns. *Angew Chem Int Ed Engl*. 2012;51(37):9297–9301. doi:10.1002/anie.201204381
13. Fan J, Chu PK. Group IV nanoparticles: synthesis, properties, and biological applications. *Small*. 2010;6(19):2080–2098. doi:10.1002/smll.201000543
14. Li W, Zhang Z, Kong B, et al. Simple and green synthesis of nitrogen-doped photoluminescent carbonaceous nanospheres for bioimaging. *Angew Chem Int Ed Engl*. 2013;52(31):8151–8155. doi:10.1002/anie.201303927
15. Chen PY, Lin AY, Lin YS, et al. Structure and mechanical properties of selected biological materials. *J Mech Behav Biomed Mater*. 2008;1(3):208–226. doi:10.1016/j.jmbbm.2008.02.003
16. Chen X, Peng LH, Chee SS, Shan YH, Liang WQ, Gao JQ. Nanoscaled pearl powder accelerates wound repair and regeneration in vitro and in vivo. *Drug Dev Ind Pharm*. 2019;45(6):1009–1016. doi:10.1080/03639045.2019.1593436
17. Liu S, Wei W, Bai Z, et al. Rapid identification of pearl powder from hyriopsis cumingii by Tri-step infrared spectroscopy combined with computer vision technology. *Spectrochim Acta A Mol Biomol Spectrosc*. 2018;189:265–274. doi:10.1016/j.saa.2017.08.031
18. Gao H, Chen H, Chen W, et al. Effect of nanometer pearl powder on calcium absorption and utilization in rats. *Food Chem*. 2008;109(3):493–498. doi:10.1016/j.foodchem.2007.12.052
19. Wang T, Zhan W, Zhang XF, et al. Synthesis of fluorescent carbon dots by gastrointestinal fluid treatment of Mongolia Har Gabur. *J Nanomater*. 2017;7(9):1–7. doi:10.1155/2017/8575162
20. Dallacasagrande V, Hajjar KA. Annexin A2 in inflammation and host defense. *Cells*. 2020;9(6):1499. doi:10.3390/cells9061499
21. Lim HI, Hajjar KA. Annexin A2 in fibrinolysis, inflammation and fibrosis. *Int J Mol Sci*. 2021;22(13):6836. doi:10.3390/ijms22136836
22. Scharf B, Clement CC, Wu XX, et al. Annexin A2 binds to endosomes following organelle destabilization by particulate wear debris. *Nat Commun*. 2012;3(1):755. doi:10.1038/ncomms1754
23. Li R, Tan S, Yu M, Jundt MC, Zhang S, Wu M. Annexin A2 regulates autophagy in pseudomonas aeruginosa infection through the Akt1-mTOR-ULK1/2 signaling pathway. *J Immunol*. 2015;195(8):3901–3911. doi:10.4049/jimmunol.1500967
24. He S, Li X, Li R, et al. Annexin A2 modulates ROS and impacts inflammatory response via IL-17 signaling in polymicrobial sepsis mice. *PLoS Pathog*. 2016;12(7):e1005743. doi:10.1371/journal.ppat.1005743
25. Gilmore TD. Introduction to NF-kappaB: players, pathways, perspectives. *Oncogene*. 2006;25(51):6680–6684. doi:10.1038/sj.onc.1209954
26. Shi X, Jie L, Wu P, et al. Calycosin mitigates chondrocyte inflammation and apoptosis by inhibiting the PI3K/AKT and NF-κB pathways. *J Ethnopharmacol*. 2022;297:115536. doi:10.1016/j.jep.2022.115536
27. Yang N, Wang M, Lin K, et al. Dectin-1 deficiency alleviates diabetic cardiomyopathy by attenuating macrophage-mediated inflammatory response. *Biochim Biophys Acta Mol Basis Dis*. 2023;1869(6):166710. doi:10.1016/j.bbadis.2023.166710
28. Lambertsen KL, Finsen B, Clausen BH. Post-stroke inflammation-target or tool for therapy? *Acta Neuropathol*. 2019;137(5):693–714. doi:10.1007/s00401-018-1930-z
29. Bist P, Leow SC, Phua QH, et al. Annexin-1 interacts with NEMO and RIP1 to constitutively activate IKK complex and NF-κB: implication in breast cancer metastasis. *Oncogene*. 2011;30(28):3174–3185. doi:10.1038/onc.2011.28
30. Tian X, Yang W, Jiang W, Zhang Z, Liu J, Tu H. Multi-omics profiling identifies microglial annexin A2 as a key mediator of NF-κB pro-inflammatory signaling in ischemic reperfusion injury. *Mol Cell Proteomics*. 2024;23(2):100723. doi:10.1016/j.mcpro.2024.100723
31. Longa EZ, Weinstein PR, Carlson S, Cummins R. Reversible middle cerebral artery occlusion without craniectomy in rats. *Stroke*. 1989;20(1):84–91. doi:10.1161/01.str.20.1.84
32. Bederson JB, Pitts LH, Tsuji M, Nishimura MC, Davis RL, Bartkowski H. Rat middle cerebral artery occlusion: evaluation of the model and development of a neurologic examination. *Stroke*. 1986;17(3):472–476. doi:10.1161/01.str.17.3.472
33. Abbott NJ, Patabendige AA, Dolman DE, Yusof SR, Begley DJ. Structure and function of the blood-brain barrier. *Neurobiol Dis*. 2010;37(1):13–25. doi:10.1016/j.nbd.2009.07.030

34. Carmeliet P, Jain RK. Principles and mechanisms of vessel normalization for cancer and other angiogenic diseases. *Nat Rev Drug Discov*. 2011;10(6):417–427. doi:10.1038/nrd3455
35. Morganti-Kossmann MC, Semple BD, Hellewell SC, Bye N, Ziebell JM. The complexity of neuroinflammation consequent to traumatic brain injury: from research evidence to potential treatments. *Acta Neuropathol*. 2019;137(5):731–755. doi:10.1007/s00401-018-1944-6